RESEARCH ARTICLE | JANUARY 03 2025

Photon number-resolving aluminum kinetic inductance detectors

X. Dai; H. Wang; Y. Wang; Z. Mai; Z. Shi; Y.-F. Wang; H. Jia; J. Liu; Q. He; M. Dai; P. Ouyang; Y. Chai; L.-F. Wei; L. Zhang; Y. Zhong; W. Guo; S. Liu; D. Yu

Appl. Phys. Lett. 126, 012602 (2025)
https://doi.org/10.1063/5.0234649

Applied Physics Letters ARTICLE pubs.aip.org/aip/apl

Photon number-resolving aluminum kinetic inductance detectors

Cite as: Appl. Phys. Lett. **126**, 012602 (2025); doi: 10.1063/5.0234649
Submitted: 22 August 2024 · Accepted: 21 December 2024 ·
Published Online: 3 January 2025

X. Dai,[1] H. Wang,[2] Y. Wang,[1,a)] Z. Mai,[1] Z. Shi,[1] Y.-F. Wang,[1] H. Jia,[2] J. Liu,[2] Q. He,[3] M. Dai,[3] P. Ouyang,[3] Y. Chai,[3] L.-F. Wei,[3] L. Zhang,[4] Y. Zhong,[2,5] W. Guo,[2,a)] S. Liu,[2,5] and D. Yu[2,5]

AFFILIATIONS

[1]Quantum Optoelectronics Laboratory, School of Physical Science and Technology, Southwest Jiaotong University, Chengdu 610031, China
[2]International Quantum Academy, Shenzhen 518048, China
[3]Information Quantum Technology Laboratory, School of Information Science and Technology, Southwest Jiaotong University, Chengdu 610031, China
[4]School of Electronic Science and Engineering, Nanjing University, Nanjing 210023, China
[5]Shenzhen Institute for Quantum Science and Engineering, Southern University of Science and Technology, Shenzhen 518055, China

[a)]Authors to whom correspondence should be addressed: qubit@swjtu.edu.cn and guoweijie@iqasz.cn

ABSTRACT

We study the multi-photon energy resolution and demonstrate photon counting up to about 30 photons at near-infrared wavelengths in a kinetic inductance detector made from aluminum (Al) film. The detector has a lumped-element design comprising a large interdigitated capacitor in parallel with a narrow inductive strip. A fiber-coupled lens is used to focus the light onto the inductive absorber to minimize photon scattering. Detectors with different designs and film thicknesses are studied. From the histogram of the optimally filtered multi-photon response pulse height, we find that the square of the energy resolution of the n-photon peak ΔE_n^2 increases linearly with the absorbed photon energy $nh\nu$. The detector made from a thicker Al film has a smaller slope of ΔE_n^2 with $nh\nu$, suggesting lower phonon loss in a thicker absorber. We also discuss other factors that limit the energy resolution and maximum resolvable photon number, including the dark noise and position-dependent response.

Photon number-resolving (PNR) and energy-resolving detectors at visible and near-infrared (NIR) wavelengths have important applications in quantum information processing and astronomical detection. Superconducting detectors have been extensively studied to serve as high-performance PNR and energy-resolving detectors due to their low noise and high sensitivity. For example, the transition edge sensors (TESs) have demonstrated high-efficiency PNR and energy-resolving performance at NIR wavelengths.[1–3] Photons can also be counted at high speed in quasi-PNR detectors based on multiplexed superconducting nanowire single-photon detectors (SNSPDs),[4–7] although a single SNSPD has no intrinsic energy-resolving capability.

Alternative PNR and energy-resolving superconducting detectors also include kinetic inductance detectors (KIDs),[8] which are made from high-quality factor superconducting micro-resonators.[9] KIDs are mainly considered for sensitive power detection in astronomy at millimeter and submillimeter wavelengths because they are easy to multiplex into large arrays. KIDs have intrinsic PNR and energy-resolving power since the resonance frequency shift is proportional to the number of generated quasi-particles from Cooper-pair breaking, which is proportional to the absorbed photon energy in the inductive absorber. Many experiments have shown photon number and energy resolution at visible to near-infrared wavelengths using KIDs.[10–15] Recently some important progresses have been made in improving the energy-resolving power of KID toward the Fano limit.[16] In Ref. 17, the authors report the best energy-resolving power of KID so far by suspending NbTiN-Al hybrid resonators on SiN_x membranes and find that hot phonon losses can significantly reduce the energy-resolving power. The energy-resolving power can also be improved in a non-membrane KID made of an indium/hafnium bilayer with the hafnium layer as a phonon blocking layer between the absorber and substrate.[18]

Previous studies mainly focus on single-photon resolution. For example, we showed a single-photon energy resolution of ≈ 0.22 eV

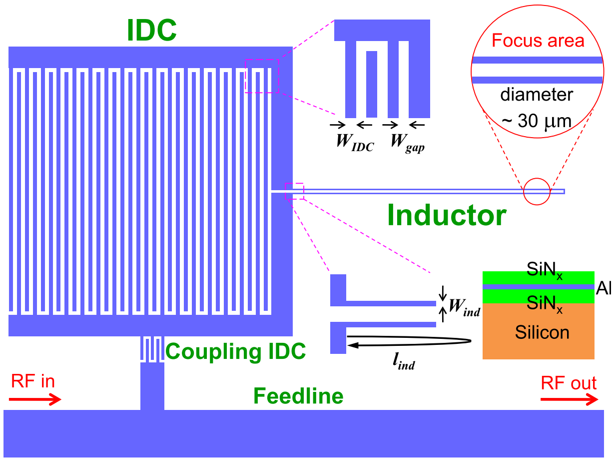

FIG. 1. Schematic drawing (not to scale) of the lumped-element resonator showing an IDC (with equal finger and gap width $w_{IDC} = w_{gap}$) shunted by an inductor strip (with width w_{ind} and length l_{ind}). The resonator is coupled to feedline by a coupling IDC and the coupling quality factor is designed to be $Q_c \approx 20 \times 10^3$. Typical design parameters: $w_{IDC} = 10\,\mu$m, $w_{ind} = 1\,\mu$m, and $l_{ind} = 1500\,\mu$m. The IDC area is $\approx 1 \times 1$ mm^2. The red circle illustrates the focused light spot with a FWHM diameter $\approx 30\,\mu$m, which is measured at room temperature with a 1064 nm laser diode.

and photon number resolving up to seven photons at 1550 nm in a TiN/Ti/TiN trilayer KID.[15] In this Letter, we study the multi-photon energy resolution and demonstrate photon counting up to about 30 photons at NIR wavelengths in a KID made from pure aluminum (Al). Our detector is based on a lumped-element resonator (Fig. 1), which allows for the light to be focused onto the inductive strip by a fiber-coupled lens. We characterize the single-photon detection performance for detectors with different resonator designs and film thicknesses (Table I). By measuring the optical pulse response of the detector illuminated by the laser light of 1064 and 1550 nm wavelengths (Fig. 2), we obtain the histogram of multi-photon response pulse height (Fig. 3). We find that the square of the energy resolution of n-photon peak ΔE_n^2 increases linearly with the absorbed photon energy $nh\nu$ (Fig. 4), where n is the photon number and $h\nu$ is the single-photon energy. In addition, the detector made from thicker Al film shows a smaller slope of ΔE_n^2 with $nh\nu$, showing the signature of phonon loss effect. We also discuss the contributions to energy resolution and maximum resolvable photon number from other factors, including the dark noise and non-uniform position-dependent response (Fig. 5).

Our detector is made from a thin Al film on a high-resistivity and double-polished silicon (Si) substrate. We deposit silicon nitride (SiN_x) layers on both the top and bottom of the Al film, because our devices with double SiN_x layers show better energy-resolving power compared to bare Al film devices. The details of the device fabrication and DC properties of the Al film are given in the supplementary material (Sec. A). As shown in Fig. 1, the detector has a lumped-element resonator design, comprising of a large interdigitated capacitor (IDC) shunted by a narrow one-turn inductive strip as the photon absorber. The resonance frequency of the resonator is designed to be ≈ 1 GHz, so that the inductor length is much shorter than the microwave wavelength and the current distribution along the inductor is uniform. A fiber-coupled lens is used to focus the light onto one end of the inductor, in order to minimize photon scattering, lower the response from IDC, and improve the detection efficiency. The details of our fiber-to-detector alignment technique are shown in the supplementary material (Sec. B). Because of the current uniformity and the illuminated position being about 0.7 mm from the IDC, the position-dependent response is expected to give a negligible contribution to degrade the energy resolution.

The detectors are cooled in a dilution refrigerator with a base temperature of 50 mK. A laser diode driven by a function generator at room temperature is used to generate optical pulses with a width of 200 ns at a repetition frequency of 120 Hz. The linewidth of the laser source corresponds to a single-photon-resolving power $R_1 > 600$. The incident photons are then attenuated, guided into the detector holder, and focused onto the inductor strip by a fiber-coupled lens. A standard homodyne scheme is used to read out the resonators. The excitation microwave power is chosen to be 3 dB below the bifurcation power[19] to maximize the signal-to-noise ratio and avoid the strong nonlinear effects. We first do a frequency sweep centered at the resonance frequency f_r to obtain the resonance circle in the complex plane [blue dots in Fig. 2(a)]. Then we probe the resonators at f_r and measure the detector response to the input optical pulse [red curve in Fig. 2(a)]. For each optical pulse, the detector response is digitized at a sampling rate of 2.5 Ms/s. We use a rigorous nonlinear fitting procedure[20] to convert the phase change $\delta\theta$ to the fractional frequency shift $\delta f_r/f_r$ [Fig. 2(b)], because $\delta f_r/f_r$ is proportional to the number of generated quasi-particles[21] while $\delta\theta$ saturates at higher optical power. The measurement setup and sequence diagram are shown in detail in the supplementary material (Sec. C).

The pulse response data are further optimally filtered to generate the photon-counting statistics from 2×10^4 pulse events. Similar results are obtained by using various optimal filters, including the standard Weiner optimal filter,[22] the Weiner filter with different template

TABLE I. Overview of the main design and measured parameters. The measured parameters include (from left to right): resonance frequency (f_r), internal quality factor (Q_i), single-photon responsivity $[(\delta f_r/f_r)_{n=1}]$, the standard deviation of the fractional resonance frequency shift in the dark (σ_0), the 0-photon energy resolution (ΔE_0), the single-photon energy resolution (ΔE_1), the single-photon energy-resolving power (R_1), and an energy resolution coefficient (J_*). The coupling quality factors (Q_c) for all detectors are $\approx 30 \times 10^3$. The presented ΔE_1 and R_1 correspond to experiments with 1064 nm photon.

Detector	Thickness (nm)	W_{IDC} (μm)	l_{ind} (μm)	f_r (GHz)	Q_i [$\times 10^3$]	$(\delta f_r/f_r)_{n=1}$	σ_0	ΔE_0 (eV)	ΔE_1 (eV)	R_1	J_*
A	25	5	3000	0.774	27.9	8.70×10^{-7}	1.37×10^{-7}	0.43	0.46	2.51	13.1
B	15	10	1500	0.793	27.8	6.26×10^{-6}	3.98×10^{-7}	0.17	0.25	4.66	22.5
C	25	10	1500	1.035	23.2	1.66×10^{-6}	1.28×10^{-7}	0.22	0.28	4.12	14.9
D	40	10	1500	1.133	19.8	5.28×10^{-7}	5.70×10^{-8}	0.30	0.36	3.26	11.3

pulses, and a convolution filter.[23] The details of the pulse filtering procedure are given in the supplementary material (Sec. D).

We fabricate and study four types of detectors. The main design and measured parameters are summarized in Table I. Detectors A and C are both made from a 25 nm thick Al film. Compared to detector A, detector C has a larger IDC with $w_{IDC} = 10\,\mu$m and a shorter inductor with $l_{ind} = 1500\,\mu$m. As expected, detector C has a lower dark noise (σ_0) and higher single-photon responsivity $[(\delta f_r/f_r)_{n=1}]$ due to its larger IDC and smaller inductor. Detectors B, C, and D have the same resonator design and the only difference lies in the Al film thickness. We can see that detector D (40 nm) has the lowest noise while detector B (15 nm) has the largest responsivity. All detectors have a moderate single-photon energy-resolving power $R_1 = E_1/\Delta E_1 \approx 2.5$–$4.7$, where $E_1 = h\nu \approx 1.17$ eV (0.8 eV) is the single-photon energy of 1064 nm (1550 nm) wavelength and ΔE_1 is the single-photon energy resolution in units of electron volt. In the following, we mainly use the data from detector C to demonstrate the photon-counting experiments because of its lower noise and higher responsivity.

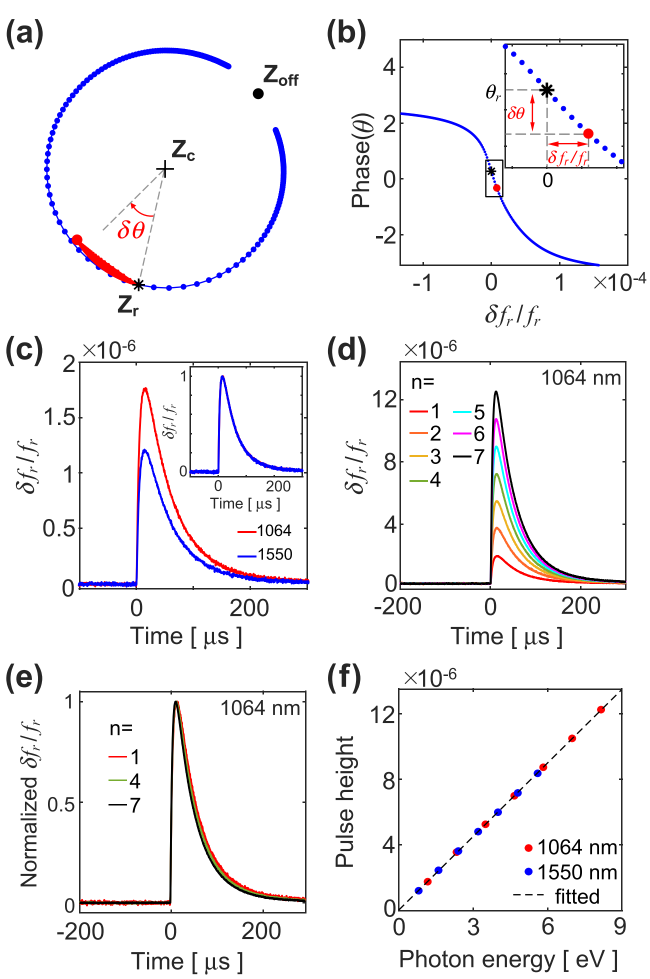

FIG. 2. (a) Resonance circle (S_{21}) centered at Z_c and averaged response pulse (red curve). Z_r is the resonance point where the frequency response $|\delta S_{21}/\delta f_r|$ is maximized. (b) Phase angle as a function of the resonance frequency shift. (c) The averaged single-photon response pulses as a function of time for 1064 and 1550 nm photons. The inset shows the normalized single-photon response pulses. (d) The averaged multi-photon response pulses for 1064 nm photons. (e) The normalized response pulses for different photon numbers. (f) The response pulse height is proportional to the absorbed photon energy.

The averaged single-photon response pulses of detector C to 1064 and 1550 nm photon are shown in Fig. 2(c). The inset shows that the normalized single-photon response pulses have the same shape with a response time $\approx 16\,\mu$s and relaxation time $\approx 56\,\mu$s, determined by the resonance circuits[24] and the properties of Al film, respectively. The averaged multi-photon response pulses to 1064 nm photons with absorbed photon number $n = 1$–7 are shown in Fig. 2(d). The normalized multi-photon response pulses are shown in Fig. 2(e), showing that the normalized response pulses for different photon numbers also have similar pulse shape, although the pulse for $n = 7$ relaxes a bit faster than the pulse for $n = 1$. Figure 2(f) shows the frequency response pulse height (peak amplitude) with the absorbed photon energy $nE_1 = nh\nu$, demonstrating a linear relation with a slope of $\approx 1.5 \times 10^{-6}$/ eV. This also suggests that a single photon with energy $nh\nu$ and n photons with single-photon energy $h\nu$ lead to the same frequency response.

Figures 3(a)–3(c) show the histograms of the optimally filtered pulse height data for 2×10^4 response pulses to 1064 nm photons at different optical power levels from low to high. In Fig. 3(a), we can clearly see four peaks, corresponding to the events of $n = 0$, 1, 2, and 3 photons being absorbed in the detector. The histogram can be fitted by a model of superposition of n-photon Gaussian peaks with independent heights A_n and width σ_n, which are shown by the red curves. The FWHM energy resolution ΔE_n (in units of electron volt) of the n-photon peak can be determined from the fitted standard deviation σ_n by

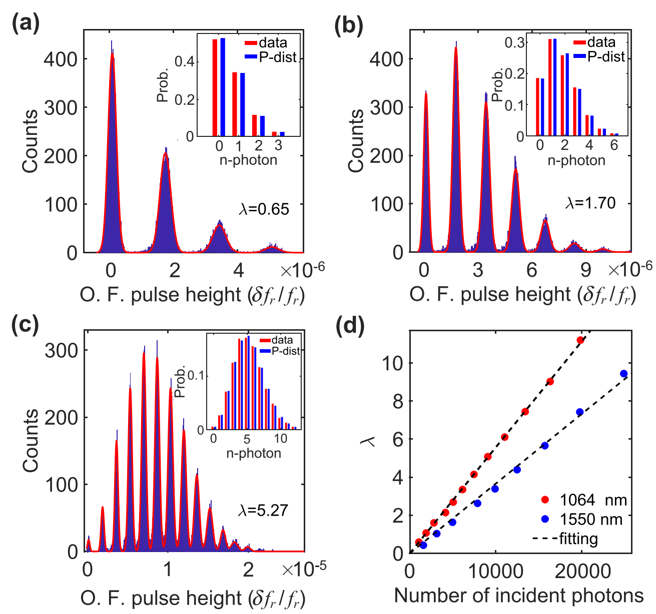

FIG. 3. Histogram of the optimally filtered (O. F.) pulse height for different mean absorbed photon number: (a) $\lambda = 0.65$, (b) $\lambda = 1.70$, and (c) $\lambda = 5.27$. The insets show that the photon number distribution follow Poisson statistics. (d) λ is linear with the number of incident photons at both 1064 and 1550 nm wavelengths.

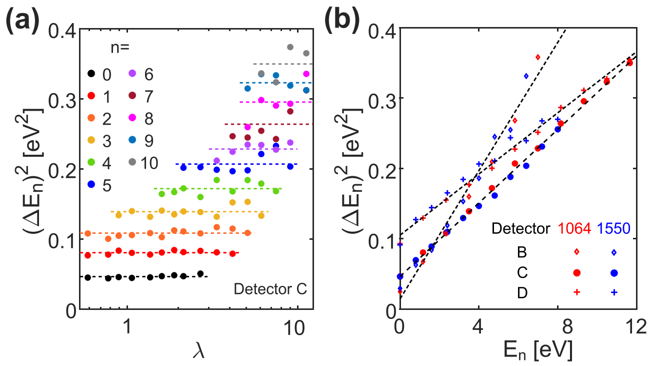

FIG. 4. (a) The fitted ΔE_n^2 as a function of λ for $n = 0$–10 at 1064 nm (detector C). The average values of ΔE_n^2 are marked by the dashed lines. (b) For all detectors (B, C, and D), the averaged ΔE_n^2 exhibits a linear relationship with absorbed photon energy. Detector D with a 40 nm thick Al film shows the smallest slope of ΔE_n^2 with E_n.

$$\Delta E_n = 2\sqrt{2\ln(2)}\frac{\sigma_n}{\left(\frac{\delta f_r}{f_r}\right)_{n=1}}h\nu, \tag{1}$$

where $(\delta f_r/f_r)_{n=1} = A_1 - A_0$ is the single-photon responsivity. The obtained ΔE_n for the four photon peaks in Fig. 3(a) are $\Delta E_0 = 0.22$ eV, $\Delta E_1 = 0.28$ eV, $\Delta E_2 = 0.33$ eV, and $\Delta E_3 = 0.37$ eV, respectively. The inset of Fig. 3(a) shows the probability of n-photon events, which are derived from the counts in the n-photon peak normalized by the total counts and agree well with a Poisson distribution with $\lambda = 0.65$. Here, λ is the mean photon number detected by the detector, suggesting that an average of 0.65 photons is absorbed in the detector per pulse. With increasing optical power, more photon peaks show up, which can be seen in Figs. 3(b) and 3(c), corresponding to Poisson distribution with $\lambda = 1.70$ and $\lambda = 5.27$, respectively.

Figure 3(d) shows the mean absorbed photon number λ as a function of the number of incident photons into the detector holder, which is linear as expected. We estimate the photon number from the input power of the laser diode and the attenuation along the optical paths measured by a power meter at room temperature. Note that a few decibel errors may occur in this estimation. From the slope we can obtain the total detection efficiency $\approx$0.056% (0.037%) for 1064 nm (1550 nm) photons, which can be explained by considering a Gaussian light spot with a FWHM diameter $\approx$198 μm (177 μm) and $\approx$8% (4.5%) absorption efficiency in the Al film.[25] The derived light spot diameter at low temperature is much larger than the value measured at room temperature, which may attribute to the misalignment due to the position changing of the light spot.

From Fig. 3, we observe that the width of the n-photon peak is slowly broadened as n increases. To further investigate this phenomenon, we plot the fitted ΔE_n^2 with λ for $n = 0$–10 in Fig. 4(a). We can see that ΔE_n has little optical power dependence for lower n. With increasing n, the fluctuation in ΔE_n^2 becomes larger because as more photons are observed in the histogram, the number of data points within each photon peak decreases, resulting in a larger uncertainty in the fitting. In Fig. 4(b), we plot the averaged ΔE_n^2 at different powers with the absorbed photon energy $E_n = nh\nu$ for both 1064 and 1550 nm photons. The data points of both wavelengths fall onto the same line, demonstrating a linear relation of ΔE_n^2 with $nh\nu$. For comparison, we show data for detectors B and D in Fig. 4(b), also demonstrating the linear relation between ΔE_n^2 and $nh\nu$ with different slopes.

Many factors can lead to the broadening of ΔE_n with the absorbed photon energy, and these factors may mainly include the dark noise, the non-uniform response, and the phonon loss effect. Assuming these factors are independent, then we write $\Delta E_n^2 = \Delta E_{ns}^2(n) + \Delta E_{rsp}^2(n) + \Delta E_{ph}^2(n)$. $\Delta E_{ns}(n)$ is the energy resolution of the n-photon peak due to dark noises from different sources (e.g., the amplifier noise). $\Delta E_{ns}(0) = \Delta E_0$ is the energy resolution of the 0-photon peak, which is proportional to the frequency noise amplitude at the resonance frequency. For a given phase noise level $\delta\theta$ (voltage noise), the frequency noise $\delta f_r = \delta\theta/(\mathrm{d}\theta/\mathrm{d}f_r)$ increases as away from the resonance point, where $\mathrm{d}\theta/\mathrm{d}f_r$ is maximized. Therefore, $\Delta E_{ns}(n)$ is expected to increase with $nh\nu$. The estimated $\Delta E_{ns}^2(n)$ is given by the black curve in Fig. 5(a), showing that $\Delta E_{ns}^2(n)$ increases slowly with $nh\nu$ and contributes less than 5% to the experimental ΔE_n^2. Under ideal conditions (e.g., perfect fabrication), the current is uniform along the inductor, and the simulated energy resolution due to position-dependent response $\Delta E_{rsp} \approx 0$ ($R_1 > 4000$), which is negligible. The energy resolution due to phonon loss is given by $\Delta E_{ph}(n) = 2\sqrt{2\ln(2)\Delta(F+J)nh\nu/\eta_{pb}^{\max}}$, where $\Delta = 0.18$ meV is the superconducting energy gap, $F \approx 0.2$ is the Fano factor, $\eta_{pb}^{\max} \approx 0.59$ is the maximum energy conversion efficiency, and J is the phonon loss factor.[17] The absolute value of J can be obtained by calculating the variance of the hot phonon energy losses in the downconversion process from photon energy to quasi-particles.[26] For our case of Si substrate and front side illumination, J is estimated to be ≈ 3.2 (for detector C) and the corresponding $\Delta E_{ph}^2(n)$ is given by the green curve in Fig. 5(a). See the supplementary material (Secs. E–G) for details on the estimation of $\Delta E_{ns}(n)$, $\Delta E_{rsp}(n)$, and J factor, respectively.

From above analysis, the phonon loss effect is expected to be dominant in the broadening of ΔE_n. The dashed lines in Fig. 4(b) show the linearly fitted ΔE_n^2 with the photon energy to a model

$$\Delta E_n^2 = \Delta E_0^2 + 8\ln(2)\Delta J_* nh\nu/\eta_{pb}^{\max}, \tag{2}$$

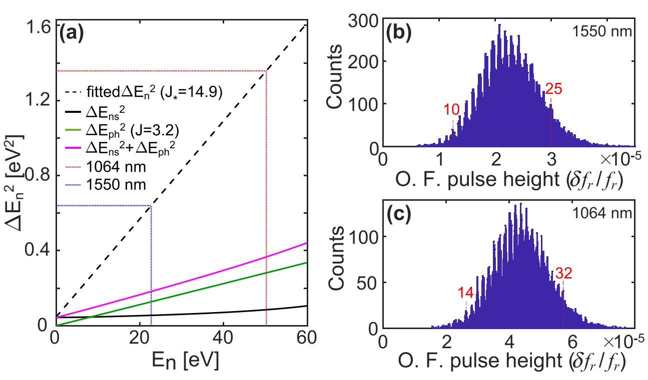

FIG. 5. (a) Estimated $\Delta E_{ns}^2(n)$ and $\Delta E_{ph}^2(n)$ for detector C. The dashed line is the fitted $\Delta E_n^2(n)$ in experiments. (b) Photon-counting histogram for 1550 nm photons at high optical power. (c) Photon-counting histogram for 1064 nm photons at high optical power. The method to determine the photon number of each photon peak is described in detail in Sec. H in the supplementary material.

where the second term takes the same form as the contribution from phonon loss and J_* is a fitting parameter representing the slope of measured ΔE_n^2 with $nh\nu$. From fitting, we obtain $J_* \approx (22.5, 14.9, 11.3)$ for detectors (B, C, and D), showing that the detector made from a thicker Al film has a smaller J_*. With typical material parameters, we can calculate the phonon loss factors $J \approx (5.6, 3.2, 1.2)$ for detectors (B, C, and D). We find that both J_* and J decrease with increasing thickness of the Al film, consistent with the fact of lower phonon loss in thicker metal film. However, the difference between J_* and J is large. We think one possible reason is the underestimation of J, because the J-calculation [Eq. (S3) in the supplementary material] is sensitive to several variables, e.g., the mean free path of phonons and phonon transmission coefficient at the interface. Increasing the input values of these variables will result in a larger J. For example, by increasing the mean free path of Debye phonons from 12.8 nm[27] to 25.6 nm, we obtain $J \approx (8.1, 5.4, 3.1)$ for detectors (B, C, and D). Another possible reason is the position-dependent response due to the imperfect sample fabrication (e.g., non-uniform width and thickness of the inductor), and thinner film may have greater non-uniformity. However, according to analysis in the supplementary material (Sec. F), ΔE_n^2 with $nh\nu$ should have different slopes for 1064 and 1550 nm photons if non-uniform response is a leading factor. This contradicts with experimental result, therefore, it is unlikely that non-uniform response has a significant contribution.

Another interesting question is what is the maximum number of photons that can be resolved, i.e., the dynamic range of the photon-counting detector. If we define the criterion for resolving the n-photon as $\Delta E_n < E_1 = h\nu$, and assume that ΔE_n^2 is linear with $nh\nu$ throughout the range, then the maximum resolvable photon number is given by

$$n_{max} = \frac{\eta_{pb}^{max}}{8\ln(2)\Delta J_*}\left(h\nu - \frac{\Delta E_0^2}{h\nu}\right). \quad (3)$$

For 1550 and 1064 nm photons, we obtain $n_{\max} = 27$ and $n_{\max} = 42$, corresponding to the blue and red dotted lines in Fig. 5(a). Figures 5(b) and 5(c) show the photon-counting histograms for 1550 and 1064 nm photons at high optical powers. Due to the large number of peaks and their overlap, it is difficult to accurately fit the width of each photon peak and obtain energy resolution. However, we can see up to 25 distinct photon peaks in Fig. 5(b) for 1550 nm photons, agreeing well with the calculated $n_{\max} = 27$. However, for 1064 nm photons, the observed number of photon peaks ≈ 32, which is less than the predicted $n_{\max} = 42$, indicates that the experimental ΔE_n^2 may have a non-linear relation with $nh\nu$ in a higher photon energy regime and thus degrades faster.

In conclusion, we measure the multi-photon responses of lens-coupled kinetic inductance detectors made from pure aluminum film with thickness 15–40 nm. From the histogram of the optimally filtered multi-photon response pulse height, we obtain the energy resolution of n-photon peak ΔE_n and find that ΔE_n^2 increases linearly with the absorbed photon energy $nh\nu$ in a wide range. Detector made from thinner Al film shows smaller single-photon energy resolution but larger slope of ΔE_n^2 with $nh\nu$, which can be partially explained by the phonon loss effect, dark noise, and non-uniform position-dependent response. These factors limit our detectors to observe up to about 30 photon peaks in the photon-counting statistics at NIR wavelengths.

See the supplementary material for details on device fabrication, fiber-to-detector coupling technique, optical pulse response measurement, optimal pulse filtering, calculation of $\Delta E_{ns}(n)$, $\Delta E_{rsp}(n)$, and J factor, and the photon number determination of photon peak in the histogram.

This work was supported in part by the National Natural Science Foundation of China (Grant Nos. 61871333, 62001204, and 11974290) and the National Key Research and Development Program of China (No. 2022YFC2205000). We thank Dr. J. Gao and Dr. Pieter J. de Visser for very useful discussions.

AUTHOR DECLARATIONS

Conflict of Interest

The authors have no conflicts to disclose.

Author Contributions

X. Dai and H. Wang contributed equally to this work.

X. Dai: Formal analysis (equal); Investigation (equal); Writing – original draft (equal). **H. Wang:** Formal analysis (equal); Investigation (equal); Writing – original draft (equal). **Y. Wang:** Formal analysis (equal); Investigation (equal); Project administration (lead); Supervision (equal). **Z. Mai:** Formal analysis (supporting); Investigation (supporting). **Z. Shi:** Formal analysis (supporting); Investigation (supporting). **Y.-F. Wang:** Formal analysis (supporting); Investigation (supporting). **H. Jia:** Investigation (supporting). **J. Liu:** Investigation (supporting). **Q. He:** Formal analysis (supporting); Investigation (supporting). **M. Dai:** Formal analysis (supporting); Investigation (supporting). **P. Ouyang:** Investigation (supporting). **Y. Chai:** Investigation (supporting). **L.-F. Wei:** Investigation (supporting); Supervision (supporting). **L. Zhang:** Investigation (supporting). **Y. Zhong:** Investigation (supporting). **W. Guo:** Formal analysis (equal); Investigation (equal); Supervision (equal); Writing – review & editing (equal). **S. Liu:** Investigation (supporting). **D. Yu:** Investigation (supporting).

DATA AVAILABILITY

The data that support the findings of this study are available from the corresponding authors upon reasonable request.

REFERENCES

[1] A. Lita, A. Miller, and S. Nam, Opt. Express **16**, 3032 (2008).
[2] B. Calkins, P. Mennea, A. Lita, B. Metcalf, W. Kolthammer, A. Linares, J. Spring, P. Humphreys, R. Mirin, J. Gates, P. Smith, I. Walmsley, T. Gerrits, and S. Nam, Opt. Express **21**, 22657 (2013).
[3] P. Li, J. Zhong, W. Zhang, Z. Wang, Q. Ma, Z. Feng, W. Miao, Y. Ren, J. Li, Q. Yao, and S. Shi, J. Low Temp. Phys. **214**, 100 (2024).
[4] F. Mattioli, Z. Zhou, A. Gaggero, R. Gaudio, R. Leoni, and A. Fiore, Opt. Express **24**, 9067 (2016).
[5] H. Hao, Q. Zhao, L. Kong, S. Chen, H. Wang, Y. Huang, J. Guo, C. Wan, H. Liu, X. Tu, L. Zhang, X. Jia, J. Chen, L. Kang, C. Li, T. Chen, G. Cao, and P. Wu, Appl. Phys. Lett. **119**, 232601 (2021).
[6] R. Cheng, Y. Zhou, S. Wang, M. Shen, T. Taher, and H. Tang, Nat. Photonics **17**, 112 (2023).
[7] T. Zhang, J. Huang, X. Zhang, C. Ding, H. Yu, Y. Xiao, C. Lv, X. Liu, Z. Wang, L. You, X. Xie, and H. Li, Photonics Res. **12**, 1328 (2024).

[8] P. K. Day, H. G. LeDuc, B. A. Mazin, A. Vayonakis, and J. Zmuidzinas, Nature **425**, 817 (2003).
[9] J. Zmuidzinas, Annu. Rev. Condens. Matter Phys. **3**, 169 (2012).
[10] J. Gao, M. Vissers, M. Sandberg, F. Silva, S. Nam, D. Pappas, D. Wisbey, E. Langman, S. Meeker, B. Mazin, H. Leduc, J. Zmuidzinas, and K. Irwin, Appl. Phys. Lett. **101**, 142602 (2012).
[11] N. Zobrist, G. Goiffard, B. Bumble, N. Swimmer, S. Steiger, M. Daal, G. Collura, A. Walter, C. Bockstiegel, N. Fruitwala, I. Lipartito, and B. A. Mazin, Appl. Phys. Lett. **115**, 213503 (2019).
[12] R. Mezzena, M. Faverzani, E. Ferri, A. Giachero, B. Margesin, A. Nucciotti, A. Puiu, and A. Vinante, J. Low Temp. Phys. **199**, 73 (2020).
[13] K. Kouwenhoven, D. Fan, E. Biancalani, S. Rooij, T. Karim, C. Smith, V. Murugesan, D. Thoen, J. Baselmans, and P. Visser, Phys. Rev. Appl. **19**, 034007 (2023).
[14] F. Boussaha, J. Hu, P. Nicaise, J. Martin, C. Chaumont, P. Dung, J. Firminy, F. Reix, P. Bonifacio, M. Piat, and H. Geoffray, Appl. Phys. Lett. **122**, 212602 (2023).
[15] W. Guo, X. Liu, Y. Wang, Q. Wei, L. F. Wei, J. Hubmayr, J. Fowler, J. Ullom, L. Vale, M. R. Vissers, and J. Gao, Appl. Phys. Lett. **110**, 212601 (2017).
[16] U. Fano, Phys. Rev. **72**, 26 (1947).
[17] P. Visser, S. Rooij, V. Murugesan, D. Thoen, and J. Baselmans, Phys. Rev. Appl. **16**, 034051 (2021).
[18] N. Zobrist, W. Clay, G. Coiffard, M. Daal, N. Swimmer, P. Day, and B. Mazin, Phys. Rev. Lett. **129**, 017701 (2022).
[19] L. Swenson, P. Day, B. Eom, H. Leduc, N. Llombart, C. McKenney, O. Noroozian, and J. Zmuidzinas, J. Appl. Phys. **113**, 104501 (2013).
[20] X. Dai, X. Liu, Q. He, Y. Chen, Z. Mai, Z. Shi, W. Guo, Y. Wang, L. Wei, M. Vissers, and J. Gao, Supercond. Sci. Technol. **36**, 015003 (2023).
[21] J. Gao, J. Zmuidzinas, A. Vayonakis, P. Day, B. Mazin, and H. Leduc, J. Low Temp. Phys. **151**, 557 (2008).
[22] S. R. Golwala, Ph.D. thesis (University of California, Berkeley, CA, 2000).
[23] B. K. Alpert, R. D. Horansky, D. A. Bennett, W. B. Doriese, J. W. Fowler, A. S. Hoover, M. W. Rabin, and J. N. Ullom, Rev. Sci. Instrum. **84**, 056107 (2013).
[24] J. Hu, Q. He, F. Yu, Y. Chen, M. Dai, H. Guan, P. Ouyang, J. Han, C. Liu, X. Dai, Z. Mai, X. Liu, M. Zhang, L. F. Wei, M. R. Vissers, J. Gao, and Y. Wang, Appl. Phys. Lett. **119**, 022601 (2021).
[25] Z. Mai, X. Dai, Y. Chen, Z. Shi, H. Wang, C. Pan, X. Liu, Z. Wang, W. Guo, and Y. Wang, Appl. Opt. **62**, 5294 (2023).
[26] A. Kozorezov, J. Wigmore, D. Martin, P. Verhoeve, and A. Peacock, Phys. Rev. B **75**, 094513 (2007).
[27] A. G. Kozorezov, A. F. Volkov, J. K. Wigmore, A. Peacock, A. Poelaert, and R. den Hartog, Phys. Rev. B **61**, 11807 (2000).